Use of Derivative Calculations and Minimum Noise Fraction Transform for Detecting and Correcting the Spectral Curvature Effect (Smile) in Hyperion Images

Alon Dadon, Eyal Ben-Dor, and Arnon Karnieli, *Member, IEEE*

***Abstract*—Earth Observing-1 Hyperion data were found to be relatively noisy and to contain significant cross-track spectral curvature nonlinearity disturbances, known as the *smile/frown* effect. A method for the correction of spectral curvature effects (smile) in Hyperion images, termed *trend line smile correction* (TLSC), is presented. The method is based on the assumption that there is a partial correlation between data spectral nonuniformity, due to the smile and eigenvalues gradient that mostly appears in the first minimum noise fraction (MNF) image (MNF-1). However, MNF-1 consists of both spatial and spectral information. Therefore, it is hypothesized that adaptation applied to MNF-1, according to exclusively spectrally derived parameters (e.g., atmospheric absorption features) can account specifically for the smile effect in the data. A set of normalization factors, calculated from the spectral derivative at the right-hand side of the O_2 absorption feature (760 nm), MNF-1 and the moderate-resolution atmospheric transmittance radiative transfer model, are used to scale the initial MNF-1. The image is corrected after the inverse conversion of the MNF to radiance space. The methodology was tested on four different Hyperion scenes and consistently outperformed other tested methods by up to nine times. As a result, thematic mapping, using the TLSC-corrected reflectance data cube, was shown to be consistent with the geology maps of the study area.**

***Index Terms*—Geological classification, Hyperion Earth Observing 1 (EO-1), hyperspectral remote sensing, smile effect, spectral derivative.**

I. Introduction

VARIOUS pushbroom imaging spectroscopy systems experience low-frequency array effects that are often referred to as the spectral *curvature effect*, or *smile/frown* and *keystone* interferences [1], [2]. These effects depend on the position of each cell on the charge-coupled device (CCD) array, relative to the imaging optics' center axis. The keystone effect refers to changes within the spatial cell dimension (lower than the pixel size), whereas the smile effect refers to changes within the spectral dimension (lower than the bandwidth size) [1]. While the keystone effect is difficult to account for and correct, the smile effect is significant in the spectral domain [3].

The sources of the smile effect are ascribed to the optical techniques used to disperse the input imaged "slit" in the wavelength dimension over the detector grid. The detector elements in a pushbroom system are arranged on a rectilinear grid, therefore dispersing the slit onto the straight rows of detector elements leads to spatial misalignment of the wavelength and bandwidth [4], [5]. Smile may also be a product of aberrations in the collimator and imaging optics [4]. The spectral curvature may affect the proper retrieval of surface reflectance [6], particularly in the spectral regions affected by sharp gaseous absorption features, which demand high spectral accuracy for effective atmospheric correction [7]. As most common atmospheric correction methods apply a radiative transfer model to the data, it is highly important to have the data centered at the exact band position [6]–[8]. Since the smile effect may render spectral absorption positions, the resulting atmospheric correction may be insufficient, leading to a noisy reflectance product; consequently, the thematic spectral-based products may be erroneous [9], e.g., thematic misclassification of the data.

The Hyperion hyperspectral sensor onboard the Earth Observing-1 (EO-1) spacecraft is a pushbroom imaging spectrometer [10]–[12]. Hyperion consists of 242 bands at bandwidth of approximately 10-nm full-width at half-maximum (FWHM). The instrument's swath is 7.5 km, containing 256 columns (pixels) with 30-m spatial resolution. Hyperion comprises two grating spectrometers; one covering the visible near-infrared (VNIR) wavelength range (357–1055 nm), with a silicon CCD and another HgCdTe detector, covering the short-wave infrared (SWIR) range (851–2576 nm). The signal reaches the Hyperion detectors through a single telescope and slit with a dichroic filter to split the signal into the two spectrometers [3]. Early results from selected Hyperion validation sites in the U.S. (e.g., [13]), Argentina (e.g., [14] and [15]), Australia (e.g., [16]), Botswana (e.g [17]), and Eritrea (e.g., [18]) showed that the system generally performed correctly and produced useful geologic (mineralogical/lithological) information. Nevertheless, it was reported that Hyperion data had drawbacks, such as relatively low signal-to-noise ratios (SNR) [6], spectral and spatial artifacts related to the array malfunction, and a significant smile effect [6], [12], [14], [16], [19], [20].

Laboratory measurements performed prior to the launch of the system indicated that the smile effect is dependent on

Manuscript received July 11, 2009; revised November 18, 2009. Date of publication March 4, 2010; date of current version May 19, 2010. This work was supported in part by the Ramon scholarship awarded by the Israeli Ministry of Science, Culture, and Sport and in part by the International Sephardic Education Foundation.

A. Dadon and A. Karnieli are with the Remote Sensing Laboratory, Jacob Blaustein Institutes for Desert Research, Ben-Gurion University of the Negev, Beersheba 84990, Israel (e-mail: dadonalo@bgu.ac.il; karnieli@bgu.ac.il).

E. Ben-Dor is with the Remote Sensing and GIS Laboratory, Department of Geography and Human Environment, Tel Aviv University, Tel Aviv 69978, Israel (e-mail: bendor@post.tau.ac.il).

Color versions of one or more of the figures in this paper are available online at http://ieeexplore.ieee.org.

Digital Object Identifier 10.1109/TGRS.2010.2040391

the pixel position (column) in the cross-track direction of the Hyperion image and on different magnitudes at the VNIR and SWIR detectors [21]. Throughout the Hyperion operations, peak-to-peak smile differences of less than 1 nm have been observed in the SWIR wavelengths and 2.6–4.25 nm in the VNIR detector wavelengths [6], [20]. Considering the high spectral resolution of the Hyperion output (10.0–11.5 nm), such spectral differences in the VNIR are significant and cannot be ignored for further analysis [20]. Moreover, the smile effect may vary from one image to another [20]. Therefore, it is not possible to use prelaunch correction functions. Due to Hyperion malfunctions and low SNR, not much experience has been gained with the instrument and the smile effect remains a considerable challenge for the scientific community [4], [10], [22].

The smile effect in Hyperion data is not evident in a single band, since the spectral shifts are less than a bandwidth. Therefore, detecting the smile effect in the data is not a trivial task. The smile effect becomes apparent in spectral calibration stages in terms of sensitivity of radiance measurements in spectral regions with sharp radiance changes (e.g., atmospheric absorption features). Several studies [5], [7], [15], [23] demonstrated how the relatively homogeneous absorption features of atmosphere gasses may serve as indicators for the smile effect.

Soon after the EO-1 launch, a brightness variation in the minimum noise fraction (MNF) transformations [24] (normally the first MNF is referred to as MNF-1) was noticed [4]. It was particularly apparent in the VNIR range, which presented a similar shape to models describing the "smile/frown" effect. Accordingly, the MNF-1 was used as a smile indicator in various studies (e.g., [4], [9], and [16]). However, according to [4] and [9], MNF-1 compares spatial and spectral information and is therefore not designed for the sole purpose of smile detection.

Although the problem of removing the smile effect from the raw data has drawn considerable attention, most of the developed methodologies dealing with smile (e.g., [6], [9], [25], and [26]) were reported as partial, in some cases, complex and not applicable for the common user in others, and commonly causing perturbation of the spectra.

A. Previous Smile Considerations

The first smile correction applied to Hyperion data was performed by Thompson Ramo Wooldridge (TRW), Inc. (now Northrop Grumman Space Technology) and was based on a prelaunch characterization of spectral and spatial variation of the Hyperion detector arrays, as reported by [21]. The prelaunch measurements were used to calculate the repositioning of band centers for proper atmospheric correction. In practice, it was found that the TRW correction factors did not properly correct the smile effect and, in fact, some significant errors were even increased in several spectral regions, such as the first few VNIR bands [6]. This effect may be explained by possible postlaunch changes in the spectral calibration [6], [9]. It is not yet clear why the changes occurred, although [12] reported that it may be due to a problem that occurred during the integration of the sensor into the EO-1 platform.

The traditional way of detecting and correcting the smile effect takes into account the gray scale cross-track drift of the MNF-1 band image, in some cases by applying a polynomial smoothing correction to MNF-1 band [16] and in others, its complete elimination. However, these techniques are limited, due to variations in the surface albedo that contribute errors to the correction function. The smile is then poorly corrected, while other information may be lost [4].

To the best of the authors' knowledge, the only atmospheric removal software that attempts to consider smile in the process is the high-accuracy atmospheric correction for hyperspectral data model, developed at the Center for the Study of Earth from Space, University of Colorado at Boulder [27], [28]. However, it does not directly perform radiance smile correction, rather than detecting smile at atmospheric absorption features and then performing atmospheric correction per-column accordingly. Moreover, this software is not yet available to most users, who commonly utilize such packages as environment for visualizing images (ENVI) fast line-of-sight atmospheric analysis of spectral hypercubes [29], Atmospheric Correction Now (ACORN) [30], atmospheric correction [31], [32], or other empirical-based approaches that do not properly deal with the smile issue.

Other approaches reported are related to matching of measured and modeled radiance spectra, oriented to reduce spikes in the derived reflectance near atmospheric absorptions [20], [25], [33]. Such models operate by resetting band centers and FWHM of the data, rather than directly correcting the spectra. Most of these models are complex and cannot be applied by the common user.

One of the available techniques, implemented prior atmospheric correction, is the "cross-track illumination correction" module [34], provided within the ENVI software [35]. In this module, along-track mean values are calculated and put together to evaluate variation in the cross-track direction of the scan. A polynomial function, with the order defined by the user, is fitted to the means and used to remove the variation. Cross-track illumination variations may be due to vignetting effects, instrument scanning, or other nonuniform illumination effects often observed in pushbroom instruments. As this is the only available method to deal with pushbroom affects, it is a necessary step in the correction methodology of Hyperion data, and as such, it is brought herein as a reference for comparison.

Another technique is the polynomial fit corrections applied to the MNF-1 band [4]. Here, a polynomial fit is set according to the columns average in the MNF-1 band and then applied for correcting the entire image (for each pixel). However, these two techniques only partially or indirectly remove the smile effect and may alter the spectra [4].

B. Objective

In most cases, the end-user of Hyperion data faces difficulties in detecting and correcting the spectral distortion caused by the smile effect. This may lead to erroneous data analysis (e.g., misclassification). Whereas some suggest that the smile effect is considered to be an inherent part of the data and do not include its correction within the preprocessing steps, in the authors' view, a procedure to evaluate and correct the smile effect is

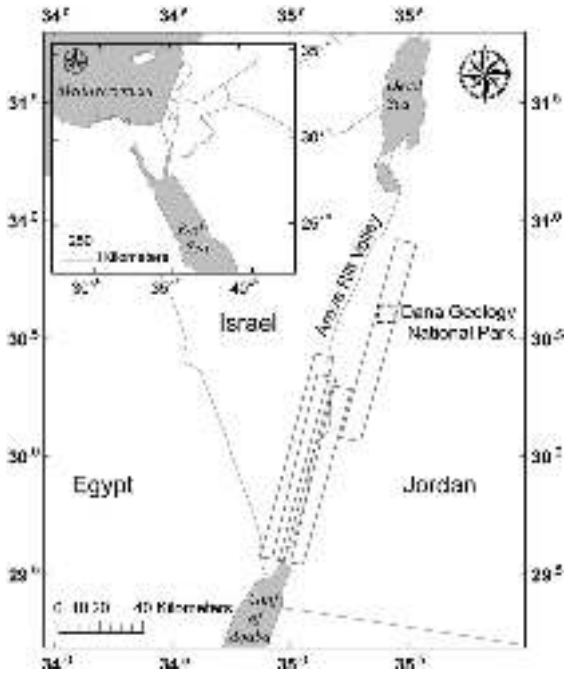

Fig. 1. Location of the four Hyperion images (Ki, Ke, Kk, and Kz) and the location of the Dana Geological National Park.

essential, and a scene-based method to tackle this problem must be developed.

Therefore, the prime objective of this paper is to explore the behavior of the smile effect in Hyperion data sets, to suggest a new method to minimize its effects and to examine the results in three stages: 1) a spectral match to moderate resolution atmospheric transmittance (MODTRAN) radiative transfer model [36]; 2) comparison to other common correction methods; and 3) examination of thematic classification. It should be noted that trend line smile correction (TLSC) is currently restricted only to the present case study and to the acquisition conditions as presented ahead.

II. Material and Methods

A. Research Area

The research was conducted over the Arava Rift Valley (also known as the Dead Sea Transform), located in southern Israel and Jordan (Fig. 1). The arid climatic conditions of the research site are characterized by precipitation of less than 50 mm annually, little cloud cover, and intense radiation throughout the year. These conditions result in low vegetation cover and very well exposed lithology and consequently, the area is very suitable for remote sensing implementation, particularly for examining the proposed correction method of the smile effect for surface thematic mapping applications. Particularly, the research area includes the Dana Geology National Park (Fig. 1). Geologically, this site comprises rock formations ranging from Precambrian to Quaternary, including both igneous and sedimentary rocks, characterized by a mineralogical assembly composed of various clay and alteration minerals. The stratigraphy of the park was mapped by [37] and the lithology, mineralogy, and land forms are well documented (e.g., [38]–[42]). The topography of the research area is generally flat to moderate with height differences of up to 700 m.

B. Data Preprocessing

Four Hyperion images, covering the vicinity of the Arava Rift Valley were used for developing the proposed methodology. These images (referred hereafter as Kz, Kk, Ke, and Ki) (Fig. 1) are of different dates, location, and viewing angles. Furthermore, the view angles diverse from east to west in several images and from west to east in others. In order to achieve significant spectral signatures of the ground features, several preprocessing steps were applied, including radiometric calibration, noise reduction, and atmospheric correction.

The radiometric calibration was performed according to the manufacturer's instructions [36]. Noise reduction operations were then applied, in order to remove artifacts related to bad pixel phenomena and other factors for improving data SNR [14], [19], [43]. The striping effect, resulting from the Hyperion pushbroom system (bad pixels), was corrected by using a local destriping approach. Bad pixels were located and removed by using the nearest neighbor algorithm [6], [14], [16]. MNF transformation was applied to segregate noise from the data [8]. These noise-reducing procedures, however, were not set to remove the smile effect, to be discussed in the next section. Hence, the data were not yet subjected to atmospheric correction.

C. Smile Correction Approach

Any smile correction methodology must consist of at least three stages: 1) smile detection and quantification; 2) correction of the detected cross-track variation; and 3) evaluation of the correction performance in light of the user requirements. As noted, Hyperion prelaunch smile estimates are inapplicable, as the smile appearance varies from scene to scene [20]. On the other hand, the MNF-1 gradient does not fully represent the smile effect [4]. Therefore, the smile effect must be determined according to inherent per scene indicators. Previous methods attempting to correct smile, such as column mean corrections (as in global destriping), applying a polynomial correction to the gray scale gradient in MNF-1, or even removing MNF-1 from the data and fitting low-order polynomials as in "cross-track illumination" [4], [9] are reported to result in distortion of the spectra [16]. Therefore, a precise modification to the MNF-1 band, based on the evaluation of the smile effect according to absorption features of well-mixed gases, is suggested.

The hypothesis behind this methodology takes into consideration the fact that MNF-1 consists of both spatial and spectral information. Therefore, its correction, according to exclusively spectrally derived parameters (e.g., atmospheric absorption features) will account for the smile effect in the data. Assuming that by isolating the spectral curvature effect component appearing in the first MNF and implementing a correction to it, the effect will be removed from the data during the inverse MNF stage with minimal influence on the spatial components that may contribute distortion of the spectra. The rationale of the described approach is to suggest an

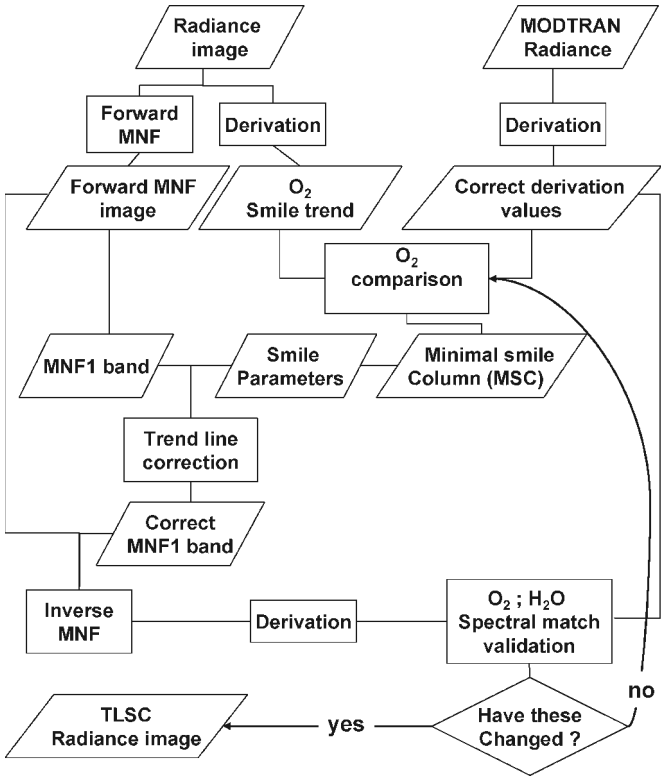

Fig. 2. Flowchart of the proposed TLSC methodology.

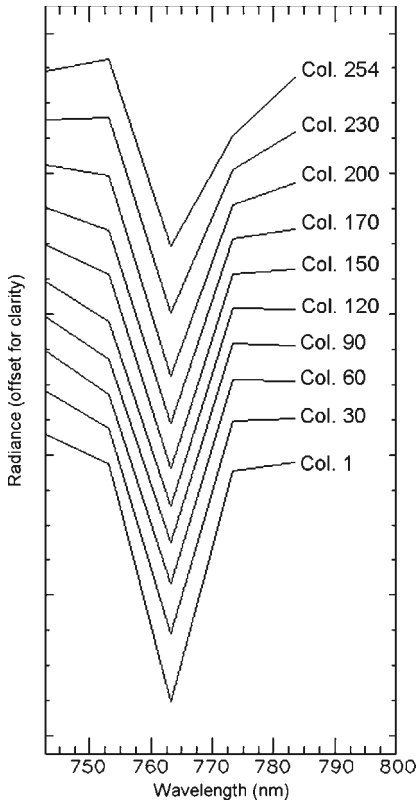

Fig. 3. O_2 absorption curves around 772 nm of selected column means, across the scene Kz. Note the change in the angle of the slopes on both shoulders of the curves.

image-based spectral correction, for the main purpose of providing smile-corrected radiance data.

In order to evaluate the validity of this image-based approach, the procedure was carried out on four different images, acquired on different dates and viewing angles. A flowchart demonstrating the methodology is shown in Fig. 2. It includes a smile detection procedure that is performed by spectral comparison of the radiance image to the radiative transfer absorptions and by locating the minimal smile column in the data. The TLSC modifies the MNF-1 band according to the calculated smile drift from the minimal smile column. The corrected MNF band is than inserted into the inverse MNF procedure, converting the coherent data back to radiance values. The final stage is a spectral comparison to MODTRAN for validation purposes.

D. Smile Detection

As previously explained (Section I-A), quantifying and correcting the smile effect in an individual image requires internal indicators. Therefore, it is necessary to define image-based parameters that will represent the smile effect as precisely as possible, beyond the MNF-1 procedures previously suggested [4], [16]. According to several works [7], [15], [23], [25], [33], absorption features of well-mixed gases, appear in both VNIR and SWIR regions (e.g., O_2 and CO_2, respectively); they are intense and lie within the relatively high-SNR spectral regions and, therefore, can be used as internal indicators for the smile effect. The well-mixed gas absorption features are limited in number; however, unlike surface features, they are relatively homogeneously spread across the image particularly in flat terrain areas [20]. Consequently, the O_2 absorption near 760 nm was used to assess the smile effect in the VNIR region, while CO_2 absorption, at 2012 nm, was used for the SWIR. It is assumed that their spectral features are relatively similar and stable across the detector line array (columns).

A direct measurement of variation in the position of the absorption features across the Hyperion data set is not feasible, since the bands are centered in fixed locations. Furthermore, as noted, the well-mixed gas absorption features are relatively homogeneous and, therefore, do not exhibit pronounced changes in depth. However, a notable change in the angle of the slopes, on both sides of the absorption curve (shoulder), was apparent at different columns across the image (Fig. 3). Therefore, in order to detect possible cross-track variation in O_2 and CO_2 absorptions due to smile, the first derivative of the right-hand side shoulders (B') was calculated per pixel as follows:

$$B' = \frac{B_2 - B_1}{\overline{\mathrm{FWHM}}} \tag{1}$$

where B_1 is an absorption band image, B_2 is the following band image (right shoulder), and $\overline{\mathrm{FWHM}}$ is the average FWHM of these two bands. The calculation was applied to both O_2 and CO_2 absorption band images for all four scenes.

When examining the column mean derivative values of the O_2 (i.e., $B_1 = 772$-nm band and $B_2 = 782$-nm band) and CO_2 band images (i.e., $B_1 = 2012$-nm band and $B_2 = 2022$-nm band), shown in Fig. 4(a)–(d), the cross-track nonlinearity variation is seen for O_2 average cross sections, as typically

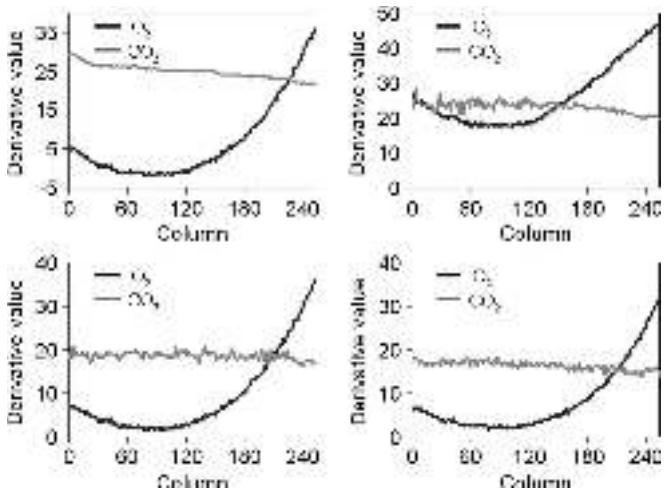

Fig. 4. Column mean derivative values of O_2 around 772 nm and CO_2 around 2012-nm band images of Kz, Kk, Ke, and Ki scenes (a, b, c, and d, respectively).

obtained from the gray scale scene in MNF-1 band images. In all data sets, O_2 derivative values vary on both sides of the image and particularly, on the right-hand side. These findings demonstrate the nonsymmetric nature of the smile effect and its relation to the spatial location in the image (the field of view). Fig. 4 also suggests that in all four data sets, the smile effect is mostly dominant in the VNIR region, while the CO_2 derivative column mean displays only random noise, rather than significant cross-track nonlinearity variations. This stands in good agreement with other findings reported for the Hyperion data (e.g., [5], [20], and [21]). Based on these results, the steps detailed below were applied to the VNIR spectral region alone.

One of the challenges for correcting smile in an individual scene is determining which columns of the image are not disturbed by smile, referred hereinafter as *minimal smile columns* (MSC). Being an image-based correction, the smile detection method described here is based on the cross-track variance from the minimal smile column. For that purpose, O_2 absorption features across the image were correlated with MODTRAN O_2 absorption features. MODTRAN radiance spectral absorptions were calculated for the time and location of the Hyperion scenes acquisition. Input information for MODTRAN included the Sun's azimuth, elevation, and zenith and the horizontal visibility (all obtained from Aeronet data of the region). Bright sand reflectance taken *in situ* (used also for EL) was chosen as background spectra (pixel). As the comparison between image reflectance and MODTRAN at sensor reflectance was done specifically to the gas absorption regions and by using a local derivative, no normalization had to be applied other than spectral resampling according to the Hyperion VNIR sensor.

Comparison of the MODTRAN derivative values and the image-based ones detected the location of the MSCs at columns 173, 32, 46, and 85 for the Kz, Kk, Ke, and Ki images, respectively. The MSCs served as reference factors in the correction methodology. Other authors have described similar smile detection methodologies that utilize atmospheric absorption features [5], [20], [25], [26], [33]. However, the technique described here differs from these methods, both in the detection and correction approaches as will be further discussed in the flowing section.

E. TLSC

The conditioning of the data in the correction methodology involved moderate adaptation to the MNF transformation. Parameters for these adaptations were derived according to the cross-track distance from the MSC mean derivative value. For that purpose, mean derivative values of O2 absorption were calculated for each column and compared to that of the MSC, formulating the smile function. A second-order polynomial function, referred hereafter as trend line (TL) was fitted to the smile function. The TL function was then scaled according to the MNF-1 values. Adaptation in the current study was simply performed by arithmetical addition and subtraction, rather than the accustomed polynomial fit [4], [9]. Moreover, the MSC was used for fine-tuning of the smile drifts. It is intended to prevent smoothing and maintain the spectral uniqueness of each pixel, while correcting the smile disturbance. Equation (2) formulates the calculation, termed hereafter as TLSC

$$\mathsf{MNF\text{-}1_{TLSC}} = \Sigma\left(\mathsf{X_{MNF}} + (-\mathsf{TL_{CX}}) \pm \Delta\mathsf{MSC}\right) \qquad (2)$$

where $\mathrm{MNF\text{-}1_{TLSC}}$ is the corrected MNF-1 band image, $\mathrm{X_{MNF}}$ is the MNF-1 band image pixel, $\mathrm{TL_{(CX)}}$ is the TL scaled to MNF values (calculated for the column at which $\mathrm{X_{MNF}}$ is located), and $\Delta\mathsf{MSC}$ is the remainder of the output column from the calculated MSC ratio.

The original MNF-1 band image, where the gray scale abnormal gradient appears [Fig. 5(a)–(d)], is then replaced by the corrected band [Fig. 5(e)–(h)]. According to the inverse MNF procedure, selected MNF bands (including the corrected MNF-1) are reconstructed backward to the radiance image domain [24]. The final stage of the TLSC is validation of the results. It is performed by comparing the obtained image derivative values with that computed for MODTRAN, by means of variance. The comparison is performed both for O_2 (672 nm) and H_2O (833 nm) absorption features' right shoulders. Thereafter, the resulting radiance TLSC image is subject to further processing, such as atmospheric correction and thematic classification.

F. Atmospheric Correction

Whereas the results of the aforementioned steps can be further used to correct the image for atmospheric attenuation by various model-based methods, in this paper, the Atmospheric Correction Now (ACORN) model [30] was used. Ground truth samples, which included different land covers and surface components of several rock types, were measured using an Analytical Spectrometer Devices field spectrometer [44], both in the field and in the laboratory. The empirical line (EL) technique [45], based on selected spectra, was used for refining the atmospheric correction. EL calibration forces the image spectra to match reflectance spectra collected from the field, specifically a dark and bright target. The targets selected for the EL correction were chosen mainly according to their cross-track location and spectral albedo. The selected bright target was

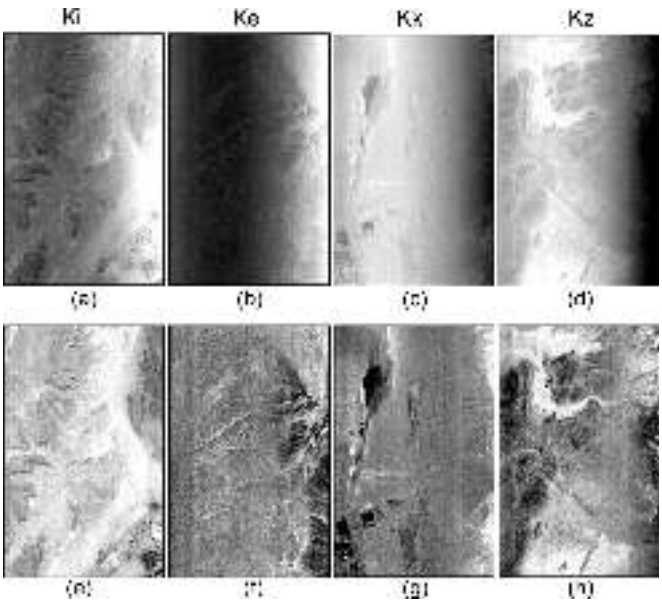

Fig. 5. Comparison between original MNF-1 band images [(a)–(d)] and the TL-corrected ones [(e)–(h)] for Kz, Kk, Ke, and Ki scenes.

sand, located in column number 10 and the dark one was porphyry granite at column 167. Both were collected from homogeneous areas and do not significantly lose their original properties due to transportation. Both locations are relatively close to the minimal smile columns. The final output product of this stage was a noise reduced reflectance Hyperion image.

G. Classification

In order to differentiate among rock formations within the research area, several classification methods embedded in ENVI software [35] were applied. The pixel purity index (PPI) [46] was used to find the most "spectrally pure" pixels (endmembers) in the image. The results of the PPI were used as input for the n-Dimensional Visualizer tool in ENVI [47]. The coordinates of the points in n-space consist of "n" values that are the spectral reflectance values in each band for a given pixel. The distribution of these points in n-space was then used to estimate the number of spectral endmembers and their pure spectral signatures. Fifteen endmembers were extracted from the aforementioned stage and introduced into the spectral angle mapper (SAM) supervised classification method [47], [48], which was applied to the images before and after correction. The SAM method uses an n-dimensional angle to match pixels to reference spectra. The advantage of this technique lies in the fact that it is relatively insensitive to illumination and albedo effects [49]. The final output product was a thematic geology map. The classification procedures were performed on both the TLSC reflectance image and a noncorrected reflectance image of the research site (both include the EL correction).

III. Results and Discussion

A. Smile Correction Results

One of the immediate outcomes of the TLSC procedure is reduction of the near atmospheric absorption spikes, as shown

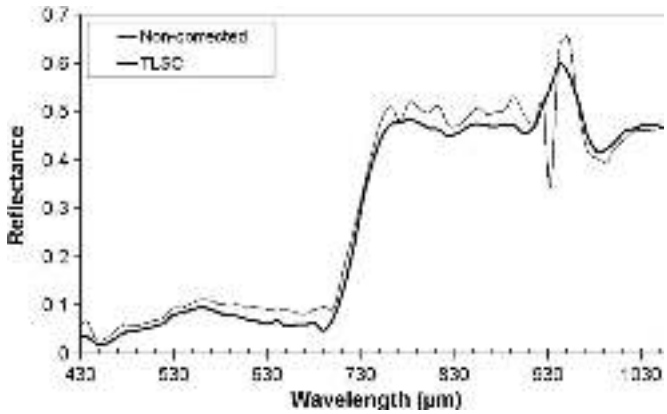

Fig. 6. Example of a VNIR reflectance spectral curve of an image pixel (Ke, x:11, Y:331) (thin line) before and (thick line) after TLSC correction. No EL or any other smoothing was applied.

in Fig. 6. This figure shows an example of a VNIR reflectance spectral curve, before and after TLSC correction and prior to the EL smoothing. Note the diminution of spikes near the atmospheric water-vapor absorptions at 940 μm, which, in current data sets, were more dominant than spikes near the 760-μm absorption.

The effectiveness and accuracy of the TLSC performance was quantified by calculating the O_2 derivative of the TLSC radiance output image and comparing it with a MODTRAN derivation of the same band. A similar analysis was also performed for H_2O absorption feature at 823 nm. In both cases, the spectral match was determined by computing the *deviation*

$$\text{Deviation} = \sqrt{(n - \text{MODTRAN}n)^2} \tag{3}$$

where n is the column's mean derivative and MODTRAN is the respective MODTRAN derivative. Therefore, lower cross-track deviation indicates less smile interference in the data. Fig. 7(a)–(d) shows O_2 spectral cross-track deviation before and after the TLSC, revealing the finding that the cross-track deviations of the corrected O_2 absorption features are, on average, seven times lower than the original for all data sets and up to 12 times lower for the right-hand side. For the H_2O absorption case [Fig. 7(e)–(h)], TLSC data sets showed a decrease in deviation by two and ten for the average and for the right-hand side, respectively. H_2O deviation values were generally higher. This may be either the outcome of abnormalities in water vapor, a miscalculation of water vapor carried out by MODTRAN for this specific data set, or a lower degree of correction for this spectral region. As the water vapor for all data sets was extracted in the ACORN atmospheric correction procedure and was found to be consistent, it is assumed that a combination of the second and the third explanations is the main reason for the higher deviation.

Results of the TLSC were also compared to available methods commonly used in the preprocessing of Hyperion data, i.e., the "cross-track illumination correction" module of ENVI, originally designed to remove the cross-track illumination variation of an image, and the polynomial smoothing correction, frequently applied to the MNF-1 band. Fig. 8 shows the cross-track deviation of derivative values of O_2 [Fig. 8(a)–(d)] and

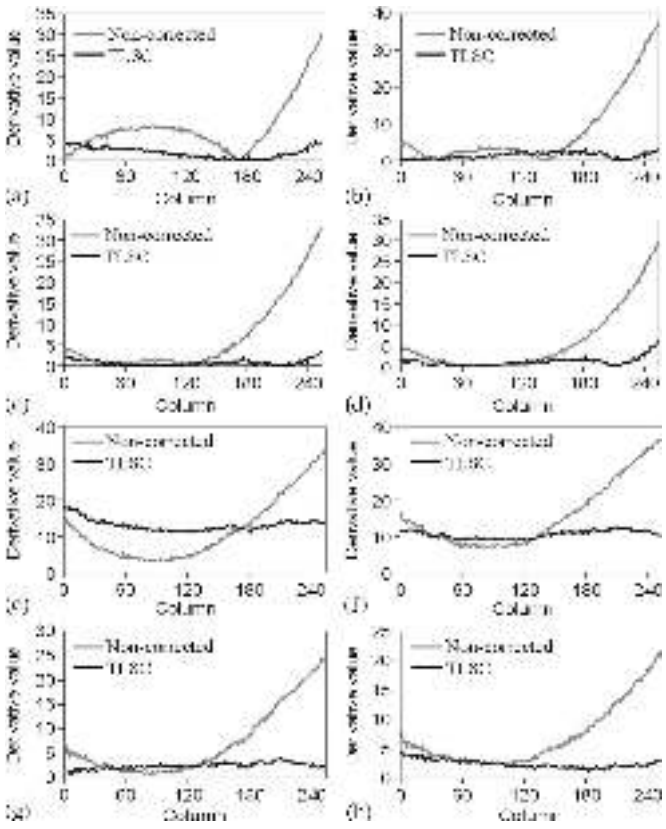

Fig. 7. Deviation of O_2 column mean derivative values (around 772 nm) from the minimal smile column value across Kz, Kk, Ke, and Ki scenes [(a), (b), (c), and (d), respectively], (in gray) before and (in black) after the TLSC. Respectively, (e)–(h) present the results for H_2O (at 823 nm).

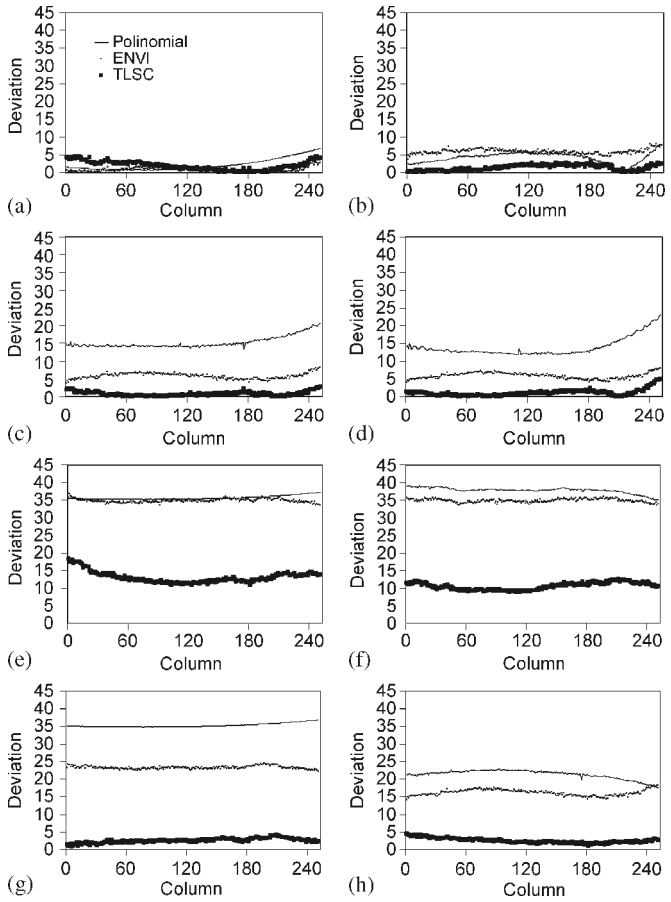

Fig. 8. Standard deviation of O_2 column mean derivative values (around 772 nm), from derivative values of the minimal smile column value across Kz, Kk, Ke, and Ki scenes [(a), (b), (c), and (d), respectively], subsequent to different smile corrections: the (gray) polynomial fit correction, the (thin black) ENVI cross-track illumination correction, and the (thick black) TL correction. Respectively, (e)–(h) present the results for H_2O (at 823 nm).

H_2O [Fig. 8(e)–(h)] from that of the minimal smile column, for the tested correction methods. The polynomial and cross-track illumination correction methods exhibit higher values of deviation compared to those derived by the proposed TLSC procedure, except for one data set (Kz), where values of the O_2 absorption were similar [Fig. 8(a)]. Quantitative values of the deviations are presented in Table I. It can be seen that, on average, the TLSC reduces the cross-track variations by a factor of eight for both absorptions. TLSC exceeded the cross-track illumination correction (ENVI) on average by a factor of six and the polynomial MNF-1 smoothing correction by a factor of nine (Table I).

Subsequent to applying the ACORN atmospheric correction in conjunction with the EL method, a final evaluation of the preprocessing effectiveness was carried out in terms of reliability of the reflectance spectra for classification of the research area. In order to verify that the main contribution to an improved classification comes from TLSC, rather than the EL correction, the comparison of classification results for the noncorrected and TLSC data sets was performed subsequent to the EL correction as well as MNF procedure.

The thematic classification procedure was first applied to VNIR reflectance images processed by ACORN and EL correction, both to the noncorrected and the TLSC images. Fig. 9 shows the core of the difficulty tackled in the current research. As can be seen, the classification results prior the TLSC procedure [Fig. 9(a)], distinguish between most of the different classes (rock types) appearing in the research area, excluding the right-hand side of the image, for which only one class was assigned. However, in the classification results of the TLSC image [Fig. 9(b)], several different classes appear. The final classification map, produced using both TLSC VNIR and the SWIR spectral regions, resembles the 1 : 50 000 geology map of the research area (mapping results will be elaborated on in a separate paper), indicating that the TLSC improves spectral reliability to a level that significantly increases the thematic mapping potential of the Hyperion data.

IV. Summary and Conclusion

Theoretically, the Hyperion data should provide improved geological information that currently cannot be obtained by any other space borne system. Nevertheless, the Hyperion data were found to be relatively noisy (average SNR of 40), in which significant smile effects were embedded that were difficult to handle by the common end-user. A straightforward method to detect and correct the smile effect is suggested in this paper. First, the VNIR and SWIR sensors were examined for the smile effect magnitude and then, a conceptually new correction method termed TLSC was applied. For the current data, only

TABLE I
DEVIATION OF THE DERIVATIVE VALUES OF O_2 ABSORPTIONS (AT 772 nm) AND H_2O ABSORPTIONS (AT 823 nm) FROM DERIVATIVE VALUE OF THE MINIMAL SMILE COLUMNS IN DIFFERENT IMAGES AND ACCORDING TO DIFFERENT CORRECTION METHODS: 1) NONCORRECTED IMAGE; 2) POLYNOMIAL CORRECTION; 3) ENVI CROSS-TRACK ILLUMINATION CORRECTION; AND 4) TLSC. AVERAGED VALUES OF BOTH THE RIGHT-HAND SIDE AND THE ENTIRE IMAGE ARE PRESENTED

Absorption feature	Correction method	Ki		Ke		Kk		Kz	
		Right	Entire	Right	Entire	Right	Entire	Right	Entire
O_2	Non corrected	30	6	33	7	37	8	30	8
	Polynomial	24	14	21	15	9	4	6	2
	ENVI	8	6	8	6	8	6	3	1
	TLSC	6	1	3	0.8	3	1	5	2
H_2O	Non corrected	22	7	37	7	37	16	34	12
	Polynomial	17	21	37	35	35	38	37	36
	ENVI	18	16	22	23	34	35	34	35
	TLSC	3	2	2	2	10	10	14	13

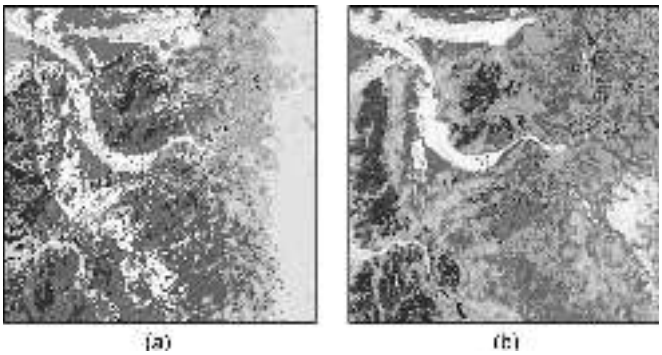

Fig. 9. VNIR-based classification after atmospheric and EL correction, for (a) nonsmile-corrected and (b) TLSC images.

the VNIR sensor was found to have a significant smile effect and therefore, this element was further studied.

The concept of TLSC is based on assessing the smile effect, using image-based cross-track derivation values of atmospheric absorption features, according to which, normalized parameters are arithmetically subtracted or added to the MNF band that embodies smile noise (commonly the first MNF). In this manner, the MNF band image was modified strictly according to image-based spectral parameters, while keeping its originality. The TLSC MNF band image was finally used to reconstruct the original radiance image to provide smile-corrected radiance data. Evaluation of the smile effect correction performance was carried out in three stages: 1) matching O_2 and H_2O absorption features across the data set with MODTRAN absorption features; 2) comparison with other commonly used methods; and 3) comparing spectral retrieval of selected targets with thematic mapping of the Dana Geology National Park area in southeastern Jordan. At each stage, the TLSC results consistently and significantly outperformed the noncorrected data and other methods tested. In addition, TLSC significantly reduces spikes near 940-nm water-vapor absorption region, implying that although TLSC does not deal directly with band-to-band smile differences, by using MNF the correction is applied to all bands.

The success of TLSC in correctly revealing geological features over four particular scenes is encouraging. It is likely that correction of Hyperion data over other homogeneous arid areas would yield positive results. It is admitted, however, that until the proposed method be successfully tested on other environments and acquisition conditions it is not robust. The TLSC should be examined for the cases of: (a) airborne imaging spectrometers; (b) low to medium smile; (c) rough terrain; and (d) in the presence of particular spatial patterns such as those of clouds or coastal lines. These all are subject to future research. Finally, it is our hope that the effectiveness of TLSC will improve the accessibility of Hyperion data and possibly, of future pushbroom hyperspectral spaceborne missions.

ACKNOWLEDGMENT

The authors would like to thank Dr. M. Beyth and Dr. O. Crouvi (Geological Survey of Israel), R. Lugasi (Tel Aviv University), and Dr. N. Panov (Jacob Blaustein Institutes) for the support and instructive advice and to A. Goldberg and M. Adar for the helpful administrative support. The authors would also like to thank the anonymous reviewers for their constructive remarks. Atmospheric attributes for this paper were obtained from Aeronet (http://aeronet.gsfc.nasa.gov).

REFERENCES

[1] P. Mouroulis, R. O. Green, and T. G. Chrien, "Design of pushbroom imaging spectrometers for optimum recovery of spectroscopic and spatial information," *Appl. Opt.*, vol. 39, no. 13, pp. 2210–2220, May 2000.

[2] C. O. Davis, M. E. Kappus, J. H. Bowles, J. Fisher, J. A. Antoniades, and M. Carney, "Calibration, characterization, and first results with the Ocean PHILLS hyperspectral imager," *Proc. SPIE*, vol. 3753, pp. 160–168, Oct. 1999.

[3] S. F. Biggar, K. J. Thome, and W. Wisniewski, "Vicarious radiometric calibration of EO-1 sensors by reference to high-reflectance ground targets," *IEEE Trans. Geosci. Remote Sens.*, vol. 41, no. 6, pp. 1174–1179, Jun. 2003.

[4] D. L. B. Jupp, B. Datt, T. R. McVicar, T. G. Van Niel, J. S. Pearlman, J. L. Lovell, and E. A. King, "Improving the analysis of Hyperion red-edge index from an agricultural area," *Proc. SPIE*, vol. 4898, pp. 1–15, Jun. 2003.

[5] R. A. Neville, L. Sun, and K. Staenz, "Detection of spectral line curvature in imaging spectrometer data," *Proc. SPIE*, vol. 5093, pp. 144–154, Sep. 2003.

[6] K. Staenz, R. A. Neville, S. Clavette, R. Landry, and H. P. White, "Retrieval of surface reflectance from Hyperion radiance data," *IEEE Geosci. Remote Sens. Lett.*, vol. 1, no. 2, pp. 1419–1421, Apr. 2002.

[7] B. Cairns, B. E. Carlson, R. X. Ying, A. A. Lacis, and V. Oinas, "Atmospheric correction and its application to an analysis of Hyperion data," *IEEE Trans. Geosci. Remote Sens.*, vol. 41, no. 6, pp. 1232–1245, Jun. 2003.

[8] R. O. Green, "Spectral calibration requirement for Earth-looking imaging spectrometers in the solar-reflected spectrum," *Appl. Opt.*, vol. 37, no. 4, pp. 683–690, Feb. 1998.

[9] D. G. Goodenough, A. Dyk, O. Niemann, J. S. Pearlman, H. Chen, T. Han, M. Murdoch, and C. West, "Processing Hyperion and ALI for forest classification," *IEEE Trans. Geosci. Remote Sens.*, vol. 41, no. 6, pp. 1321–1331, Jun. 2003.

[10] S. G. Ungar, J. S. Pearlman, J. A. Mendenhall, and D. Reuter, "Overview of the Earth Observing One (EO-1) mission," *IEEE Trans. Geosci. Remote Sens.*, vol. 41, no. 6, pp. 1149–1159, Jun. 2003.

[11] S. G. Ungar, "Technologies for future Landsat missions," *Photogramm. Eng. Remote Sens.*, vol. 63, no. 7, pp. 901–905, Jul. 1997.

[12] J. S. Pearlman, P. S. Barry, C. C. Segal, J. Shepanski, D. Beiso, and S. L. Carman, "Hyperion, a space-based imaging spectrometer," *IEEE Trans. Geosci. Remote Sens.*, vol. 41, no. 6, pp. 1160–1173, Jun. 2003.

[13] F. A. Kruse, J. W. Boardman, and J. F. Huntington, "Comparison of airborne hyperspectral data and EO-1 Hyperion for mineral mapping," *IEEE Trans. Geosci. Remote Sens.*, vol. 41, no. 6, pp. 1388–1400, Jun. 2003.

[14] G. P. Asner and K. B. Heidebrecht, "Imaging spectroscopy for desertification studies: Comparing AVIRIS and EO-1 Hyperion in Argentina drylands," *IEEE Trans. Geosci. Remote Sens.*, vol. 41, no. 6, pp. 1283–1296, Jun. 2003.

[15] R. O. Green, B. E. Pavri, and T. G. Chrien, "On-orbit radiometric and spectral calibration characteristics of EO-1 Hyperion derived with an underflight of AVIRIS and *in situ* measurements at Salar de Arizaro, Argentina," *IEEE Trans. Geosci. Remote Sens.*, vol. 41, no. 6, pp. 1194–1203, Jun. 2003.

[16] B. Datt, T. R. McVicar, T. G. Van Niel, D. L. B. Jupp, and J. S. Pearlman, "Preprocessing EO-1 Hyperion hyperspectral data to support the application of agricultural indexes," *IEEE Trans. Geosci. Remote Sens.*, vol. 41, no. 6, pp. 1246–1259, Jun. 2003.

[17] L. Bruzzone and C. Persello, "A novel approach to the selection of spatially invariant features for the classification of hyperspectral images with improved generalization capability," *IEEE Trans. Geosci. Remote Sens.*, vol. 47, no. 9, pp. 3180–3191, Sep. 2009.

[18] R. Gersman, E. Ben-Dor, M. Beyth, D. Avigad, M. Abraha, and A. Kibreab, "Mapping of hydrothermally altered rocks by the EO-1 Hyperion sensor, northern Danakil depression, Eritrea," *Int. J. Remote Sens.*, vol. 29, no. 13, pp. 3911–3936, 2008.

[19] F. A. Kruse, J. W. Boardman, and J. F. Huntington, "Comparison of EO-1 Hyperion and airborne hyperspectral remote sensing data for geologic applications," in *Proc. SPI Aerosp. Conf.*, Big Sky, MO, Mar. 9–16, 2002, vol. 6.0102, p. 12.

[20] R. A. Neville, L. Sun, and K. Staenz, "Spectral calibration of imaging spectrometers by atmospheric absorption feature matching," *Can. J. Remote Sens.*, vol. 34, pp. 29–42, 2008.

[21] L. Liao, P. Jarecke, D. Gleichauf, and R. Hedman, "Performance characterization of the Hyperion imaging spectrometer instrument," *Proc. SPIE*, vol. 4135, pp. 264–275, Nov. 2000.

[22] D. X. Kerola, C. J. Bruegge, H. N. Gross, and M. C. Helmlinger, "On-orbit calibration of the EO-1 Hyperion and Advanced Land Imager (ALI) sensors using the LED spectrometer (LSpec) automated facility," *IEEE Trans. Geosci. Remote Sens.*, vol. 47, no. 4, pp. 1244–1255, Apr. 2009.

[23] S. Delwart, R. Preusker, L. Bourg, R. Santer, D. Ramon, and J. Fischer, "MERIS in-flight spectral calibration," *Int. J. Remote Sens.*, vol. 28, no. 3/4, pp. 479–496, Feb. 2007.

[24] A. A. Green, M. Berman, P. Switzer, and M. D. Craig, "A transformation for ordering multispectral data in terms of image quality with implications for noise removal," *IEEE Trans. Geosci. Remote Sens.*, vol. 26, no. 1, pp. 65–74, Jan. 1988.

[25] B. Gao, M. J. Montes, and C. O. Davis, "Refinement of wavelength calibrations of hyperspectral imaging data using a spectrum-matching technique," *Remote Sens. Environ.*, vol. 90, no. 4, pp. 424–433, Apr. 2004.

[26] P. S. Barry, J. Shepanski, and C. Segal, "On-orbit spectral calibration verification of Hyperion," in *Proc. IEEE IGARSS*, 2001, vol. 6, pp. 2535–2537.

[27] S. Liang and H. Fang, "An improved atmospheric correction algorithm for hyperspectral remotely sensed imagery," *IEEE Geosci. Remote Sens. Lett.*, vol. 1, no. 2, pp. 112–117, Apr. 2004.

[28] Q. Zeng, B. C. Kindel, and A. F. H. Goetz, "The high accuracy atmospheric correction for hyperspectral data (HATCH) model," *IEEE Trans. Geosci. Remote Sens.*, vol. 41, no. 6, pp. 1223–1231, Jun. 2003.

[29] ENVI User's Guide, ENVI Ver. 4.1, RSI Boulder, CO, 2004.

[30] R. Green, "Atmospheric Correction Now (ACORN)," d.b.I. LLC, ed., available from Analytical Imaging and Geophysics LLC., 2001.

[31] R. Richter, "A spatially adaptive fast atmospheric correction algorithm," *Int. J. Remote Sens.*, vol. 17, no. 6, pp. 1201–1214, Apr. 1996.

[32] R. Richter and D. Schlapfer, "Considerations on water vapor and surface reflectance retrievals for a spaceborne imaging spectrometer," *IEEE Trans. Geosci. Remote Sens.*, vol. 46, no. 7, pp. 1958–1966, Jul. 2008.

[33] L. Guanter, R. Richter, and J. Moreno, "Spectral calibration of hyperspectral imagery using atmospheric absorption features," *Appl. Opt.*, vol. 45, no. 10, pp. 2360–2370, Apr. 2006.

[34] R. E. Kennedy, W. B. Cohen, and G. Takao, "Empirical methods to compensate for a view-angle-dependent brightness gradient in AVIRIS imagery," *Remote Sens. Environ.*, vol. 62, no. 3, pp. 277–291, Dec. 1997.

[35] The Environment for Visualizing Images, Res. Syst. Inc., Boulder, CO, 2008.

[36] R. Beck, "EO-1 User Guide," Version 2.3, 2003. [Online]. Available: http://eo1.usgs.gov

[37] I. Rabb'a, The Geology of the Al Qurayqira (Jabal Hamra Faddan): Map Sheet No 3051 II. Amman1994.

[38] M. Beyth, J. Henkel, and R. Geerken, Applying image processing technique and reflectance measurements combined with detailed field work for analyzing TM data of an arid area, southern Israel, vol. 11, 1998.

[39] M. Atallah, "Application of remote sensing and field techniques to tectonic problems of the dead sea rift in Jordan," Ph.D. dissertation, Technischen Univ., Munchen, Germany, 1986.

[40] F. Bender, *Geology of Jordan, Contribution to the Geology of the World*. Berlin, Germany: Gebrüder Borntraeger, 1974.

[41] S. J. McLaren, D. D. Gilbertson, J. P. Grattan, C. O. Hunt, G. A. T. Duller, and G. A. Barker, "Quaternary palaeogeomorphologic evolution of the Wadi Faynan area, southern Jordan," *Palaeogeogr. Palaeoclimatol. Palaeoecol.*, vol. 205, no. 1/2, pp. 131–154, Mar. 2004.

[42] G. Barker, O. H. Creighton, D. Gilbertson, C. O. Hunt, D. J. Mattingley, S. J. McLaren, D. C. Thomas, and G. C. Morgan, "The Wadi Faynan project, southern Jordan: A preliminary report on geomorphology and landscape archaeology," *Levant*, vol. 29, pp. 19–41, 1997.

[43] B. E. Hubbard, J. K. Crowley, and D. R. Zimbelman, "Comparative alteration mineral mapping using visible to shortwave infrared (0.4–2.4 μm) Hyperion, ALI, and ASTER imagery," *IEEE Trans. Geosci. Remote Sens.*, vol. 41, no. 6, pp. 1401–1410, Jun. 2003.

[44] ASD, Tutorial, Analytical Spectral Devices, Boulder, CO, 2002.

[45] M. Smith and E. J. Milton, "The use of the empirical line method to calibrate remotely sensed data to reflectance," *Int. J. Remote Sens.*, vol. 20, no. 13, pp. 2653–2662, Sep. 1999.

[46] J. W. Boardman, F. A. Kruse, and R. O. Green, "Mapping target signatures via partial unmixing of AVIRIS data," in *Proc. Summaries 5th JPL Airborne Earth Sci. Workshop*, 1995, pp. 23–26.

[47] J. W. Boardman, "Automating spectral unmixing of AVIRIS data using convex geometry concepts," in *Proc. 4th Annu. JPL Airborne Geosci. Workshop*, Pasadena, CA, 1993, vol. 1, pp. 11–14.

[48] J. Chen, J. Xiuping, Y. Wei, and B. Matsushita, "Generalization of subpixel analysis for hyperspectral data with flexibility in spectral similarity measures," *IEEE Trans. Geosci. Remote Sens.*, vol. 47, no. 7, pp. 2165–2171, Jul. 2009.

[49] F. A. Kruse, A. B. Lefkoff, J. W. Boardman, K. B. Heidebrecht, A. T. Shapiro, P. J. Barloon, and A. F. H. Goetz, "The spectral image processing system (SIPS)—Interactive visualization and analysis of imaging spectrometer data," *Remote Sens. Environ.*, vol. 44, no. 2/3, pp. 145–163, May/Jun. 1993.

Alon Dadon was born in 1977. He received the B.Sc. degree in geology and environmental sciences from the Ben-Gurion University of the Negev, Beersheba, Israel, in 2004 and the M.Sc. degree (*cum laude*) from the Jacob Blaustein Institutes for Desert Research, Department of Solar Energy and Environmental Physics, Ben-Gurion University of the Negev, in 2006, where he is currently working toward the Ph.D. degree.

His research interests are mainly satellite and surface-based hyperspectral remote sensing, focusing on imagine spectroscopy preprocessing and data analysis for geological applications.

Mr. Dadon is a member of the Hyperspectral Specialist Group of the Israeli Ministry of Science and Israeli Space Agency. He was awarded the "Ilan Ramon fellowship" of the Israeli Ministry of Science for a period of three years.

Eyal Ben-Dor received the Ph.D. degree from the Hebrew University of Jerusalem, Faculty of Agriculture in Soil Science, Jerusalem, Israel, in 1992.

From 1992 to 1994, he conducted a postdoctoral fellowship with the Center of Study the Earth from Space, University of Colorado at Boulder. He is a Professor with Tel Aviv University, Tel Aviv, Israel, where he was first the Chair of the Geography and Human Environment Department from 2005 to 2009 and where he is currently the Head of the Remote Sensing Laboratory within this department. He has more than 20 years experience in remote sensing of the Earth with a special emphasis on the Imaging Spectroscopy technology and soil spectroscopy. His studies focus on both quantitative and qualitative analyses of field and laboratory reflectance data and on processing of airborne and orbital hyperspectroscopy data for precise and advanced surface and atmosphere mapping of the environment.

Arnon Karnieli (M'09) received the Ph.D. degree from the University of Arizona, Tucson, in 1988.

Since then, he has been the Head of the Remote Sensing Laboratory, Jacob Blaustein Institutes for Desert Research, Ben-Gurion University of the Negev, Sede Boker Campus, Israel. His main research is focused on processing of spaceborne, airborne, and ground spectroscopic data of drylands with respect to desertification and climate change processes. He is the Israeli Principle Investigator of the forthcoming Vegetation and Environmental New Micro Spacecraft (VENμS) mission.